Geometric Analysis of Radial Basis Functions: A Differential Geometry Approach to Surface Characterization and Interpolation Performance

Mohammad Heidari^a, Maryam Mohammadi^{a,*}, Stefano De Marchi^b, Milvia Rossini^c

^aFaculty of Mathematical Sciences and Computer, Kharazmi University, Tehran, Iran ^bDepartment of Mathematics "Tullio Levi-Civita", University of Padova, Padova, Italy ^cDipartimento di Matematica e Applicazioni, Università degli Studi di Milano-Bicocca, Milano, Italy

Abstract

This paper presents a novel geometric framework for analyzing radial basis functions (RBFs) in two dimensions by interpreting them as surfaces of revolution and applying differential geometry tools to establish fundamental connections between curvature properties and interpolation performance. We derive explicit expressions for Gaussian and mean curvatures using fundamental forms, leading to a curvature-based classification that distinguishes scalable from unscalable RBFs. Our theoretical analysis reveals that scalable RBFs converge to congruent surfaces as shape parameters approach zero, with curvature convergence rates serving as fundamental predictors of practical performance. RBFs exhibiting slow curvature convergence maintain richer approximation spaces while avoiding numerical instability from excessive flattening. Through systematic examination of commonly used scalable RBFs, we establish that Matérn functions demonstrate the slowest convergence rates among both infinitely smooth RBFs (Gaussian, Multiquadric, Hyperbolic Secant, RTH) and finitely smooth compactly supported Wendland functions. Numerical experiments on challenging test problems demonstrate that the Matérn RBF achieves substantially lower errors than competing methods while maintaining stability under conditions causing catastrophic failure in Gaussian and RTH RBFs, and outperforming Wendland functions across various values of N. Additionally, unscalable RBFs such as thin plate splines and radial powers, when augmented with polynomials, exhibit inherently stable curvature behavior and provide parameter-free exact reproduction for planar surfaces. This geometric framework establishes curvature convergence analysis as an essential theoretical foundation for RBF selection and performance optimization in practical interpolation applications.

Keywords: Radial basis functions, Differential geometry, Surface of revolution, Gaussian curvature, Mean curvature

1. Introduction

Radial basis function (RBF) methods have emerged as one of the most powerful and versatile tools for scattered data interpolation and approximation, finding extensive applications across diverse scientific and engineering domains. Given a set of N scattered distinct points $\{X_j\}_{j=1}^N \subset$

^{*}Corresponding author

Email addresses: Std_M.Heidari@khu.ac.ir (Mohammad Heidari), m.mohammadi@khu.ac.ir (Maryam Mohammadi), stefano.demarchi@unipd.it (Stefano De Marchi), milvia.rossini@unimib.it (Milvia Rossini)

 \mathbb{R}^d and corresponding data values $\{f_j\}_{j=1}^N$, the RBF interpolant is constructed as

$$s(X) = \sum_{j=1}^{N} \lambda_j \phi(\|X - X_j\|), \tag{1}$$

where r = ||X|| is the Euclidean norm. $\phi(r)$ represents a radial function and the expansion coefficients λ_i are determined from the interpolation conditions $s(X_i) = f_i, j = 1, \dots, N$. This leads to the solution of a symmetric linear system $A\lambda = f$, where $A = [\phi(||X_i - X_j||)]_{1 \le i,j \le N}$, $f = [f(X_i)]_{1 \le i \le N}$. The existence of a unique solution is guaranteed for positive definite RBFs, while conditionally positive definite RBFs require the addition of lower-degree polynomials to ensure well-posedness [8, 36]. The versatility of RBF methods has led to their widespread adoption in numerous applications. Hybrid approaches combining RBFs with other techniques have proven particularly effective, such as the hybrid Gaussian-cubic RBFs for scattered data interpolation [22] and stabilized RBF finite difference methods with hybrid kernels [2, 21]. Specialized RBF formulations have been developed to handle challenging scenarios, including rational RBFs for resolving discontinuities and steep gradients [32], and stabilized interpolation using RBFs augmented with radial polynomials [27]. Recent advances have also addressed theoretical aspects, including unisolvence results for Kansa collocation methods with polyharmonic splines [23] and Multiquadric kernels for convection-diffusion problems [24]. A critical aspect of positive definite RBF based methods, is the incorporation of a shape parameter ε through the scaling $\phi(\varepsilon r)$, which fundamentally controls the behavior of the basis function. As $\varepsilon \to 0$, the RBF becomes increasingly flat, while larger values of ε produce more peaked, localized functions. This scaling mechanism creates a fundamental trade-off in RBF interpolation, it plays a crucial role both for the accuracy of the method and its stability. Although small shape parameters have been found to yield very accurate results when interpolating smooth functions [11], solving elliptic PDEs [18], and approximating data on low-dimensional manifolds within high-dimensional spaces [28], they lead to severe ill-conditioning of the interpolation matrix, potentially destroying numerical stability [9, 33]. How to handle the scaling parameter is still an open problem. A very used strategy is to choose the parameter by some optimal criteria based for instance on a variant of the cross-validation approach (leave-one-out) [29], and on its extension applied in the setting of iterated approximate moving least squares [10] or in a more general k-fold cross validation deterministic and stochastic setting [19, 20]. Further optimization and searching techniques were considered in [6, 5, 34]. The possibility of having the shape parameter vary with the translation X_j , has also been studied. This means working with functions $\phi(\varepsilon_j || X - X_j ||)$, [4, 12, 17]. A particularly important development in RBF theory has been the introduction of variably scaled kernels, where the vector case is generalized by introducing a scale function as additional coordinate. This approach, pioneered in [3], allows accommodation of the varying data characteristics in different regions of the computational domain. Variably scaled discontinuous kernels have proven especially effective for functions with edges [7], and specialized formulations have been developed for interpolating functions with gradient discontinuities [30]. Comprehensive overviews of variably scaled kernel methods highlight their growing importance in modern RBF applications [31].

The purpose of this work is to study radial basis functions in two dimensions from a geometric perspective, which provides framework to interpret their behavior and performance. While many analytical studies have compared different RBF types, the underlying geometric principles that explain their shape properties are, to our knowledge, not well investigated, leaving open

the question of how such properties can be related to performance and used to guide function selection and parameter tuning. In our previous work, we introduced a curvature-based framework for one-dimensional RBFs, showing how curvature relates to interpolation performance [15]. This provided the starting point for the two-dimensional analysis developed in the present paper. In two dimensions, the idea is to study RBFs by viewing them as surfaces of revolution in three-dimensional space. This geometric interpretation allows us to compute easily intrinsic and extrinsic curvature measures that directly characterize the "shape" of the RBFs, and to classify RBFs as scalable or unscalable according to their curvature behavior at the origin. Scalable RBFs exhibit non-zero curvatures that can be adjusted through the scale parameter such as Gaussian, Multiquadrics, Matérn and Wendland kernels, whereas unscalable RBFs, including thin-plate splines and radial powers, have curvature properties that are unaffected by scaling.

The remainder of this paper is organized as follows: Section 2 establishes the connection between RBFs and surfaces of revolution, deriving the fundamental geometric quantities including first and second fundamental forms, principal curvatures, and Gaussian and mean curvatures for RBF surfaces. Section 3 presents our main theoretical results, including the curvature-based characterization of RBFs, and detailed analysis of specific RBF families. Section 4 provides numerical validation of our theoretical findings through systematic investigation of curvature convergence rates and two challenging test problems. Finally, Section 5 concludes with a discussion of implications and future research directions. Essential concepts from differential geometry are summarized in Appendices A and B for reader convenience.

2. RBFs as surfaces of revolution

In this section, we employ concepts from classical differential geometry, assuming the reader's familiarity. The relevant basics are summarized in Appendices A and B, and further details can be found in [13, 25, 35]. Hereafter, we work with bidimensional RBFs of class at least C^2 . They can be naturally interpreted as surfaces of revolution by considering their radial symmetry about the origin. In fact $\phi(||X||)$, $X = (x, y) \in \mathbb{R}^2$ is the height function

$$z = \phi(\sqrt{x^2 + y^2}),\tag{2}$$

which can be obtained by rotating the regular parametrized planar curve $(0, |x|, \phi(|x|)), x \in \mathbb{R}$, about the z-axis. Then using cylindrical coordinates, the RBF surface of revolution $\sigma : \mathcal{U} \subseteq \mathbb{R}^2 \longrightarrow \mathbb{R}^3$ can be parametrized as

$$(r,\theta) \stackrel{\sigma}{\longmapsto} (r\cos\theta, r\sin\theta, \phi(r)),$$
 (3)

where $\mathcal{U} = (0, \infty) \times [0, 2\pi)$, $r \in [0, \infty)$ represents the radial parameter and $\theta \in [0, 2\pi)$ represents the angular parameter. In this way, we can systematically compute first and second fundamental forms, principal curvatures, Gaussian curvature, and mean curvature for any point $p = (r, \theta, \sigma(r, \theta))$. These classical geometric quantities, provide a novel lens through which to interpret RBF surfaces behavior. Since ϕ is a differentiable function, (3) forms a regular surface. Let σ_r , σ_θ , σ_{rr} , $\sigma_{r\theta}$, $\sigma_{\theta\theta}$ be the first and second order partial derivatives of σ with respect to r and θ , that for the considered revolution surface are

$$\sigma_r = (\cos \theta, \sin \theta, \phi'(r)), \quad \sigma_\theta = (-r \sin \theta, r \cos \theta, 0),$$

$$\sigma_{rr} = (0, 0, \phi''(r)), \quad \sigma_{r\theta} = (-\sin\theta, \cos\theta, 0), \quad \sigma_{\theta\theta} = (-r\cos\theta, -r\sin\theta, 0).$$

Given a point p on a regular parametric surface, the symmetric matrices corresponding to the first and second fundamental forms (\mathbf{I}_p , and \mathbf{I}_p respectively) are given respectively by

$$[\mathbf{I}_p] = \left[egin{array}{cc} E & F \ F & G \end{array}
ight], \quad [\mathbf{II}_p] = \left[egin{array}{cc} L & M \ M & N \end{array}
ight],$$

where

$$E := \langle \sigma_r, \sigma_r \rangle, \quad F := \langle \sigma_r, \sigma_\theta \rangle, \quad G := \langle \sigma_\theta, \sigma_\theta \rangle,$$

that (3) become

$$E = 1 + (\phi'(r))^2, \quad F = 0, \quad G = r^2.$$
 (4)

Here E is the square of the speed of the profile curve and hence all the meridians (r-parameter curves), while G is the square of the speed of the parallels (θ -parameter curves).

To define L, M, and N we need the normal vector at p

$$\vec{n} = \frac{\sigma_r \times \sigma_\theta}{\|\sigma_r \times \sigma_\theta\|} = \frac{(-\phi'(r)\cos\theta, -\phi'(r)\sin\theta, 1)}{\sqrt{(\phi'(r))^2 + 1}}.$$

Now

$$L := \sigma_{rr} \cdot \vec{n}, \quad M := \sigma_{r\theta} \cdot \vec{n}, \quad N := \sigma_{\theta\theta} \cdot \vec{n},$$

that in our case are

$$L = \frac{\phi''(r)}{\sqrt{(\phi'(r))^2 + 1}}, \quad M = 0, \quad N = \frac{r\phi'(r)}{\sqrt{(\phi'(r))^2 + 1}}.$$
 (5)

The matrix $[S_p] = [I_p]^{-1}[\mathbb{I}_p]$ represents the linear map S_p , known as the *shape operator*, whose eigenvalues k_1 and k_2 are real and are called the *principal curvatures* [26]. According to (4) and (5), we have

$$[S_p] = \begin{bmatrix} \frac{L}{E} & 0\\ 0 & \frac{N}{G} \end{bmatrix} = \begin{bmatrix} \frac{\phi''(r)}{((\phi'(r))^2 + 1)^{\frac{3}{2}}} & 0\\ 0 & \frac{\phi'(r)}{r\sqrt{(\phi'(r))^2 + 1}} \end{bmatrix}.$$
 (6)

Then the principal curvatures at p are given by

$$k_1 = \frac{\phi''(r)}{((\phi'(r))^2 + 1)^{3/2}},$$
 $k_2 = \frac{\phi'(r)}{r((\phi'(r))^2 + 1)^{1/2}},$

and the eigenvectors σ_r and σ_θ are principal directions at the point p. Since principal curves are defined as curves whose tangent directions at every point coincide with principal directions of the surface, we conclude that the meridians and parallels are principal curves, as their tangent vectors are in the direction of σ_r , and σ_θ , respectively. Finally, the Gaussian and mean curvatures are

$$K_g = k_1 k_2 = \frac{\phi''(r)\phi'(r)}{r((\phi'(r))^2 + 1)^2}, \quad K_m = \frac{k_1 + k_2}{2} = \frac{(\phi'(r))^3 + r\phi''(r) + \phi'(r)}{2r((\phi'(r))^2 + 1)^{3/2}}.$$
 (7)

3. Curvature-based characterization of RBFs in two dimensions

In [15], we classified RBFs, in the one-dimensional setting, into scalable and non-scalable functions, and in particular we also established the relation between the spatially varying shape parameter and the curvature. In this section, we investigate this framework in two dimensions, studying geometric behaviors related to curvatures when the scaling parameter ε is introduced.

Theorem 3.1. Let us consider the scaled parametrized RBF revolution surface

$$(r,\theta) \stackrel{\sigma_{\varepsilon}}{\longmapsto} (r\cos(\theta), r\sin(\theta), \phi(\varepsilon r)),$$
 (8)

and its Gaussian and mean curvatures at a point $p = (r, \theta, \phi(\varepsilon r))$. Then we have

$$\lim_{r \to 0} K_g = 4a_2^2 \varepsilon^4, \quad \lim_{r \to 0} K_m = 2a_2 \varepsilon^2, \tag{9}$$

where a_2 is the coefficient in (10), (11), or (12).

Proof. By using Taylor series expansion at r = 0, we have two cases. If ϕ is an infinitely smooth RBF then we have [9, Theorem 10.1]

$$\phi(\varepsilon r) = \sum_{i=0}^{\infty} a_{2i}(\varepsilon r)^{2i}.$$
 (10)

If ϕ is a finitely smooth RBF in $C^{2\delta}[0,\infty)$, $1 \leq \delta < \infty$, then we get [9, Theorem 10.2]

$$\phi(\varepsilon r) = a_0 + a_2(\varepsilon r)^2 + \dots + a_{2\delta}(\varepsilon r)^{2\delta} + a_{2\delta+1}(\varepsilon r)^{2\delta+1} + a_{2\delta+2}(\varepsilon r)^{2\delta+2} + \dots, \tag{11}$$

or

$$\phi(\varepsilon r) = a_0 + a_2(\varepsilon r)^2 + \dots + a_{2\delta}(\varepsilon r)^{2\delta} + b_{2\delta}(\varepsilon r)^{2\delta} \log(\varepsilon r) + a_{2\delta+2}(\varepsilon r)^{2\delta+2} + b_{2\delta+2}r^{2\delta+2} \log(\varepsilon r) + \dots$$
(12)

Then by substituting (10), (11), or (12) in (7), and letting $r \to 0$, the proof is complete.

As an immediate consequence of Theorem 3.1, for spatially variable scaled RBFs $\phi(\varepsilon_j || X - X_j ||)$, we have

$$K_g\left(\sigma(r,\theta)\right)\big|_{X\longrightarrow X_j} = 4a_2^2\varepsilon_j^4, \qquad K_m\left(\sigma(r,\theta)\right)\big|_{X\longrightarrow X_j} = 2a_2\varepsilon_j^2,$$

where $r = ||X - X_i||$.

Now we are ready to classify RBF surfaces according to the previous Theorem.

Definition 3.2. A radial basis surface is called scalable if it has nonzero Gaussian and mean curvatures at the origin. Otherwise, we call it unscalable.

This definition shows us, from a different perspective, the concept of flat function for RBFs depending on the scale parameter. Thus, scalability means that the mean and Gaussian curvatures at the origin are governed not only by the scale parameter, as indeed happens, but also by the coefficient a_2 , which characterizes the considered RBF. Non-scalability, instead, refers to the case where the curvature measures vanish at the origin and remain unaffected by any possible re-scaling of the radial function, i.e., they correspond to the so called shape-parameter-free functions.

Remark 3.3. From equation (9), we have $K_g \geq 0$, at the origin, for all RBFs which are at least in $C^2[0,\infty)$. This means that RBFs are never a hyperboloid surface.

Now we can state the main result of this Section related to the congruence of scalable RBFs as ε goes to zero. By the fundamental Theorem of surface theory [35], two parametrized surfaces $\sigma, \sigma^* : \mathcal{U} \longrightarrow \mathbb{R}^3$ are congruent, that is differ by the composition of a translation and a rotation if and only if their first and second fundamental forms are the same, i.e. $[I_p] = [I_p^*]$ and $[I_p] = \pm [I_p^*]$.

Theorem 3.4. All scalable RBFs are congruent to one another as the shape parameter approaches to zero.

Proof. By parameterizing any RBF surface of revolution as (8) and substituting (10), (11), or (12) in (4) and (5), and letting $\varepsilon \to 0$, we have

$$\lim_{\varepsilon \to 0} [\mathbf{I}_p] = \left[\begin{array}{cc} 1 & 0 \\ 0 & r^2 \end{array} \right],$$

and

$$\lim_{\varepsilon \to 0} \left[\mathbb{I}_p \right] = \left[\begin{array}{cc} 0 & 0 \\ 0 & 0 \end{array} \right].$$

Then according to fundamental Theorem of surface theory, the proof is complete.

It is worth emphasizing that, for scalable RBFs, the matrix $[S_p]$ tends to the zero matrix as $\varepsilon \to 0$. This behavior indicates that such functions converge to planar surfaces in the flat limit, independently of the chosen RBF. Consequently, this suggests that scalable RBFs with small shape parameters should be effective for approximating flat surfaces. However, very small shape parameters also introduce numerical instabilities, since the condition number of the interpolation matrix grows as ε decreases, which may degrade approximation accuracy in practice.

Remark 3.5. Although Theorem 3.4 establishes that all scalable RBFs are congruent as $\varepsilon \to 0$, this asymptotic result does not imply that different scalable RBFs yield similar numerical results for small finite values of ε . The congruence holds only in the mathematical limit, whereas practical computations are performed at small but non-zero shape parameters, where the functions have not yet reached their limiting behavior. The key distinction lies in the rate of convergence to the flat limit: scalable RBFs whose Gaussian and mean curvatures converge slowly to zero as $\varepsilon \to 0$ are expected to be the most effective for practical applications. The slow convergence of curvatures indicates that these functions do not become excessively flat as the shape parameter decreases. Consequently, their series expansions retain more polynomial terms compared to rapidly flattening RBFs, which helps preserve the richness of the approximation space.

3.1. Analysis of some RBF

The preceding geometric analysis provides a foundation for understanding the intrinsic curvature properties of different RBFs. To bridge the gap between our theoretical framework and practical implementation, we now specialize our curvature analysis to specific RBF families of class at least C^2 . Each RBF exhibits characteristic geometric behavior that governs its suitability for approximating surfaces with particular curvature profiles. Table 1 presents this categorization. According to Theorem Appendix A.3, all RBFs listed in Table 1 define regular surfaces, with the exception of radial powers r^{β} at the origin when $0 < \beta \le 1$.

• Powers: $\phi(r) = r^{\beta}$, $0 < \beta \notin 2\mathbb{N}$. Radial powers are C^2 at the origin for $\beta > 2$. According to (7), we have

$$K_g = \frac{(\beta - 1)\beta^2 r^{2\beta}}{(r^2 + r^{2\beta}\beta^2)^2}, \quad K_m = \frac{\beta^2 (r^{3\beta+1}\beta + r^{\beta+3})}{2r^2(r^2 + r^{2\beta}\beta^2)^{3/2}},$$

that take zero values at r=0 even in presence of a scale parameter ε . Hence they are unscalable. We also study what happens to Gaussian and mean curvatures for increasing β values. We have that for any $r \geq 0$, $\lim_{\beta \to \infty} K_g = 0$ while

$$\lim_{\beta \to \infty} K_m = \begin{cases} 0, & 0 < r < 1, \\ \frac{1}{2r}, & r \ge 1. \end{cases}$$
 (13)

This limits reveal that when $r \geq 1$, the mean curvature approaches $\frac{1}{2r}$ as β increases,

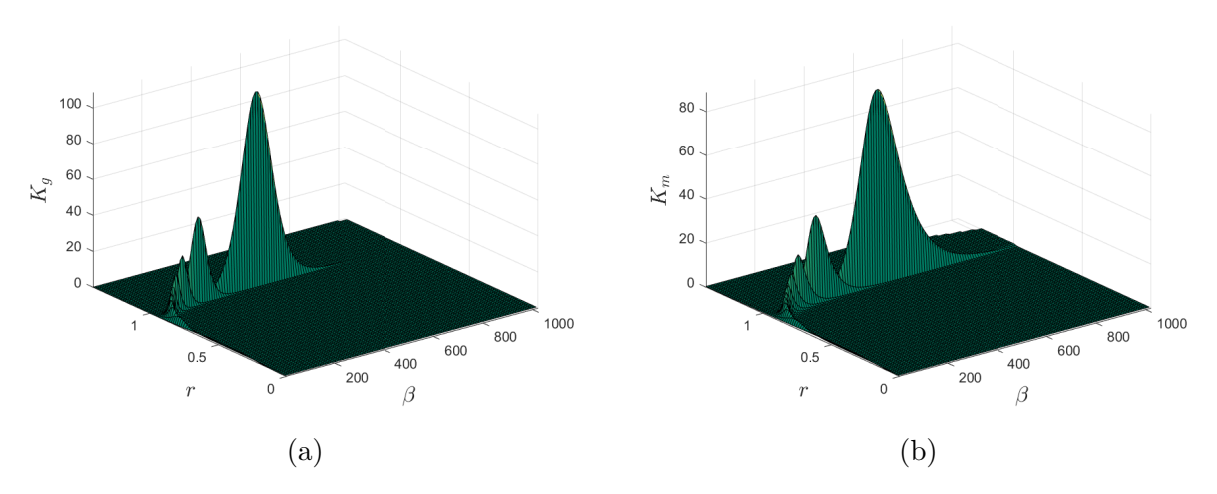


Figure 1: Gaussian (a) and mean (b) curvatures changes in radial powers with $r \in [0, \sqrt{2}]$ and $\beta \in [3, 1024]$.

while in other cases, both the Gaussian and mean curvatures converge to zero (See also Figure 1.) It is well known that, as β increases, radial power RBFs develop a flat central region. The limits we derived, however, provide additional insight: the region around r=0 that becomes flatter is effectively bounded by r<1, since the mean curvature at r=1 equals 1/2. This geometric property suggest that, when interpolation points are uniformly distributed within the domain, the resulting interpolant may attain improved accuracy in approximating planar surfaces, as each shifted RBF contributes a nearly flat region in the vicinity of its center, with an effective radius close to unity.

• Thin-plate splines (TPS): $\phi(r) = r^{2n} \log(r)$, $n \in \mathbb{N}$. TPS are C^2 at the origin for $n \geq 2$. According to (7), we have

$$K_g = \frac{r^{4n} \left((4n^2 - 2n) \ln(r) + 4n - 1 \right) \left(2n \ln(r) + 1 \right)}{16 \left(\left(n \ln(r) + \frac{1}{2} \right)^2 r^{4n} + \frac{1}{4} r^2 \right)^2},$$

$$K_m = \frac{1}{2} \frac{(4n^2 \ln(r) + 4n) r^{3+2n} + 8(n \ln(r) + \frac{1}{2})^3 r^{6n+1}}{(4(n \ln(r) + \frac{1}{2})^2 r^{4n} + r^2)^{3/2} r^2}.$$

Thus, they vanish at r=0, even in the presence of a scale parameter ε , and are therefore not scalable. Moreover, as $n\to\infty$, for any r, we obtain the following limiting behavior for the Gaussian and mean curvatures.

$$\lim_{n \to \infty} K_g = \begin{cases} 0, & 0 < r < 1, \\ \infty, & r = 1, \\ 0, & r > 1. \end{cases} \quad \lim_{n \to \infty} K_m = \begin{cases} 0, & 0 < r < 1, \\ \infty, & r = 1, \\ \frac{1}{2r}, & r > 1. \end{cases}$$
 (14)

It is not difficult to observe that, at r = 1, the growth towards infinity is linear in n. Moreover, the same considerations as for the radial powers can be applied here.

We now analyze some infinitely smooth RBFs as Gaussian, genereralized multiquadics, hyperbolic secant, RTH RBF, and some finitely smooth as Matérn and Wendland functions. The expressions of their the Gaussian and mean curvatures can be easily computed by substituting $\phi(\varepsilon r)$ into (7) and by Theorem 3.1

$$\lim_{r \to 0} K_g = 4a_2^2 \varepsilon^4, \quad \lim_{r \to 0} K_m = 2a_2 \varepsilon^2,$$

where a_2 represents the coefficient of r^2 in the series expansion of $\phi(r)$. In what follows, we compute the coefficient a_2 , which comes into play in the value of the curvature for r=0.

• Gaussian: $\phi(r) = e^{-r^2}$. Since

$$e^{-r^2} = \sum_{n=0}^{\infty} \frac{(-1)^n r^{2n}}{n!},$$

we have $a_2 = -1$.

• Generalized Multiquadrics: $\phi(r) = (1 + r^2)^{\beta}$, $\beta \in \mathbb{R} \setminus \mathbb{N}_0$ (when $\beta < 0$ are called inverse Multiquadrics). By

$$(1+r^2)^{\beta} = \sum_{k=0}^{\infty} {\beta \choose k} r^{2k},$$

we get $a_2 = \beta$. Moreover, according to (7), we have

$$K_{g} = \frac{(2\beta\varepsilon^{2})^{2} (1 + (\varepsilon r)^{2} (1 + 2(\beta - 1))) (1 + (\varepsilon r)^{2})^{2\beta - 3}}{(1 + (2\varepsilon^{2}\beta r ((\varepsilon r)^{2} + 1)^{\beta - 1})^{2})^{2}},$$

$$K_{m} = \frac{r^{2} (2\beta\varepsilon^{2} (1 + (\varepsilon r)^{2})^{\beta - 1})^{3} + 4\beta\varepsilon^{2} ((\varepsilon r)^{2} (\beta - 1) (1 + (\varepsilon r)^{2})^{\beta - 2} + (1 + (\varepsilon r)^{2})^{\beta - 1})}{2 (1 + (2\varepsilon^{2}\beta r ((\varepsilon r)^{2} + 1)^{\beta - 1})^{2})^{3/2}}.$$

Then

$$\lim_{\beta \to 0^+} K_g = \lim_{\beta \to 0^+} K_m = 0,$$

$$\lim_{\beta \to 0^-} K_g = \lim_{\beta \to 0^-} K_m = 0.$$
(15)

• **Hyperbolic Secant**: $\phi(r) = \operatorname{sech}(r)$. We have

$$\operatorname{sech}(r) = \sum_{n=0}^{\infty} \frac{E_{2n}}{(2n)!} r^{2n},$$

where E_{2n} are the Euler numbers (also called secant numbers). Then

$$\operatorname{sech}(r) = 1 - \frac{r^2}{2!} + \frac{5r^4}{4!} - \frac{61r^6}{6!} + \frac{1385r^8}{8!} - \dots$$

Therefore $a_2 = -\frac{1}{2}$.

• RTH: RTH is a new transcendental RBF of the form $\phi(r) = r \tanh(r)$ introduced for the first time by Heidari et al. [14, 15]. Now

$$r \tanh(r) = \sum_{n=1}^{\infty} \frac{2^{2n} (2^{2n} - 1) B_{2n}}{(2n)!} r^{2n},$$

where B_{2n} are the Bernoulli numbers. The first few terms are

$$r \tanh(r) = r^2 - \frac{r^4}{3} + \frac{2r^6}{15} - \frac{17r^8}{315} + \frac{62r^{10}}{2835} - \cdots$$

Then $a_2 = 1$.

• Matérn: $\phi(r) = r^{\nu} K_{\nu}(r)$, $\nu > 0$ (Matérn are C^2 at the origin for $\nu \geq 1.5$ [8]), where K_{ν} is the modified Bessel function of the second kind of order ν , that can be defined as a function of the Bessel function of the first kind as follow

$$K_{\nu}(r) = \frac{\pi}{2} \frac{J_{-\nu}(r) - J_{\nu}(r)}{\sin(\pi\nu)}, \quad J_{\nu}(r) = \left(\frac{r}{2}\right)^{\nu} \sum_{k=0}^{\infty} \frac{\left(\frac{r^2}{4}\right)^k}{k!\Gamma(\nu+k+1)}.$$

Therefore

$$\phi(r) = r^{\nu} K_{\nu}(r) = \frac{\pi}{2 \sin(\pi \nu)} \left(\frac{1}{2^{-\nu}} \sum_{k=0}^{\infty} \frac{r^{2k}}{4^k \ k! \ \Gamma(-\nu + k + 1)} - \frac{1}{2^{\nu}} \sum_{k=0}^{\infty} \frac{r^{2k+2\nu}}{4^k \ k! \ \Gamma(\nu + k + 1)} \right).$$

Then

$$a_2 = \frac{\pi}{2\sin(\pi\nu)} \cdot \frac{2^{\nu}}{4 \cdot \Gamma(2-\nu)}.$$

Now the relations

$$\Gamma(2-\nu) = (1-\nu)\Gamma(1-\nu), \quad \Gamma(\nu)\Gamma(1-\nu) = \frac{\pi}{\sin(\pi\nu)},$$

lead to

$$a_2 = \frac{2^{\nu - 3} \Gamma(\nu)}{1 - \nu}.$$

• Wendland Functions: Wendland functions are a family of compactly supported RBFs that are defined via

$$\phi_{s,k} = \mathcal{I}^k \phi_{\lfloor s/2 \rfloor + k + 1}, \ \phi_{\ell}(r) = (1 - r)_+^{\ell}$$

where \mathcal{I} is the integral operator $(\mathcal{I}f)(r) = \int_r^\infty t f(t) dt$, and $\phi_{s,k} \in C^{2k}$ [8]. These functions are all supported on [0, 1] and have a polynomial representation, there, with the degree $\lfloor \frac{s}{2} \rfloor + 3k + 1$. The most commonly used Wenland functions are given for s = 3 which are positive definite and radial on \mathbb{R}^d for $d \leq 3$.

In Table 1 the reader can find the a_2 values for the Wendland, Gaussian-Laguerre, Bump, and Poisson RBFs.

Name	Parametric Equations	a_2
Ivame	$\sigma(r,\theta) = (r\cos\theta, r\sin\theta, \phi(r))$	
Gaussian	$\phi(r) = e^{-r^2}$	-1
Gen. Multiquadrics	$\phi(r) = \left(1 + r^2\right)^{\beta}, \beta \in \mathbb{R} \backslash \mathbb{N}_0$	β
Hyperbolic Secant	$\phi(r) = \operatorname{sech}(r)$	$-\frac{1}{2}$
RTH	$\phi(r) = r \tanh(r)$	1
Bump function	$\phi(r) = \begin{cases} \exp\left(-\frac{1}{1-r^2}\right), & r < 1\\ 0, & o.w \end{cases}$	$-\mathrm{e}^{-1}$
Gaussian-Laguerre	$\phi(r) = e^{-r^2} L_n^{1/2}(r^2)$	$-\frac{4}{3}\frac{(n+\frac{3}{2})!}{\sqrt{\pi}n!}$
Poisson function	$\phi(r) = \frac{J_{\nu}(r)}{r^{\nu}}, \ \nu = \frac{d}{2} - 1, \ d \ge 2$	$-\frac{1}{2^{\nu+2}\Gamma(\nu+2)}$
Matérn/Sobolev	$\phi(r) = r^{\nu} K_{\nu}(r), \nu \ge 1.5$	$\frac{2^{\nu-3}\Gamma(\nu)}{1-\nu}$
Wendland functions	$\phi_{3,1}(r) = (1-r)_+^4 (4r+1)$	-10
	$\phi_{3,2}(r) = (1-r)_+^6 (35r^2 + 18r + 3)$	-28
	$\phi_{3,3}(r) = (1-r)_+^8 (32r^3 + 25r^2 + 8r + 1)$	-11
Powers	$\phi(r) = r^{\beta}, 2 < \beta \not\in 2\mathbb{N}$	unscalable
Thin-plate splines	$\phi(r) = r^{2n} \ln(r), 2 \le n \in \mathbb{N}$	unscalable

Table 1: Curvature-based characterization of RBFs in 3D space, with the geometric characteristic $\lim_{r\to 0} K_g = 4a_2^2 \varepsilon^4$, and $\lim_{r\to 0} K_m = 2a_2 \varepsilon^2$, where n, β , and ν are RBF parameters.

4. Numerical results

We now provide some examples that validate the key theoretical insights established in the previous sections. We show the significant role of the geometric characteristics of RBFs in accuracy and conditioning of the interpolation. We justify that the choice of RBFs and their parameters strongly depends on the function being approximated. We discuss how the choice of RBFs and tuning their shape parameters as well as the number of interpolation points can increase the accuracy while avoiding ill-conditioning. We take N uniformly distributed scattered center points in the region Ω and 51 grid points along each axis to plot the figures. We use the maximum absolute error norm $L_{\infty} = \max_{1 \leq i \leq m} |f_i - \bar{f_i}|$, where f and \bar{f} represent the exact

and approximate solutions, respectively. The 2-norm condition number is also used in all test problems.

4.1. Convergence Rates of Curvatures for Common Scalable RBFs

To investigate the curvature behavior of different scalable RBFs as the shape parameter approaches zero, we computed the convergence rates α_g and α_m for both Gaussian and mean curvatures according to power law relationships:

$$\max_{\substack{(x,y)\in\Omega}} |K_g(x,y,\varepsilon)| \sim C_g \varepsilon^{\alpha_g},$$

$$\max_{\substack{(x,y)\in\Omega}} |K_m(x,y,\varepsilon)| \sim C_m \varepsilon^{\alpha_m},$$

transformed to linear form by taking logarithms

$$\log(K_g^{\max}(\varepsilon)) = \log(C_g) + \alpha_g \log(\varepsilon),$$
$$\log(K_m^{\max}(\varepsilon)) = \log(C_m) + \alpha_m \log(\varepsilon).$$

The analysis is conducted over a sequence of decreasing shape parameters ε_k , evaluating the maximum absolute curvature values on the unit square with a uniform grid, and applying linear regression to the log-transformed data to extract the convergence rates α_g and α_m . Figure 2 presents the convergence behavior and computed rates of curvatures for commonly used scalable RBFs: Gaussian (G), Multiquadric (MQ) with $\beta = \frac{1}{2}$, Hyperbolic Secant (HS), RTH, and Matérn (MT) with $\nu = 2$. The upper panels show the logarithmic scale plots of maximum absolute curvature values as functions of ε . The lower panels provide a direct comparison of the convergence rates. For Gaussian curvature, the first four RBFs exhibit remarkably similar convergence rates of approximately 5, indicating rapid convergence to zero as ε decreases. In stark contrast, the Matérn RBF demonstrates substantially slower convergence with $\alpha_q \approx 1$, meaning its Gaussian curvature decreases at a much more gradual rate. For mean curvature, the first four RBFs show nearly identical convergence rates around 2.1, while the Matérn RBF exhibits significantly slower convergence at approximately 0.62. These results have important implications for the practical application of scalable RBFs. The Matérn RBF's slower convergence rates for both curvatures suggest that Matérn functions preserve more polynomial terms in their series expansions, thereby maintaining a richer approximation space. This characteristic makes the Matérn RBF particularly advantageous for applications requiring both numerical stability and approximation accuracy when working with small shape parameters. In Figure 3, we compare the curvature convergence rates for Matérn RBFs with $\nu = 1.5, 2, 2.5$. The results indicate that the Matérn RBF with $\nu = 2$ exhibits the slowest convergence rates, suggesting it is less susceptible to flattening in the small ε regime. Figure 4 presents the curvature convergence rates for Wendland RBFs with k = 1, 2, 3. The figure demonstrates that the Wendland RBF $\phi_{3,3}$ maintains a richer approximation space compared to the others. The curvature analysis presented in Figures 2–4 provides geometric insight into the relative performance of different RBF families in interpolation tasks. The slower curvature convergence rates observed for Matérn RBFs, particularly with $\nu = 2$, suggest superior stability properties in the flat limit, which is consistent with their well-documented practical performance advantages in numerical applications.

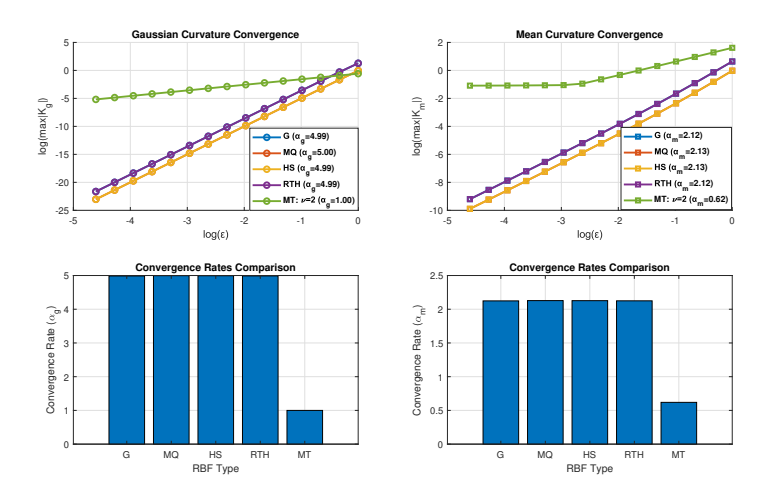


Figure 2: Convergence behavior and computed rates for common scalable RBFs.

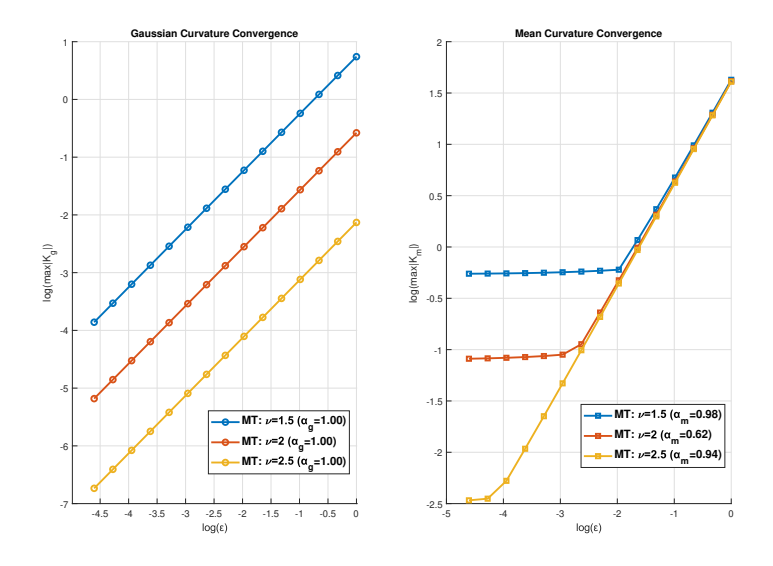


Figure 3: Convergence behavior and computed rates for Matérn RBFs.

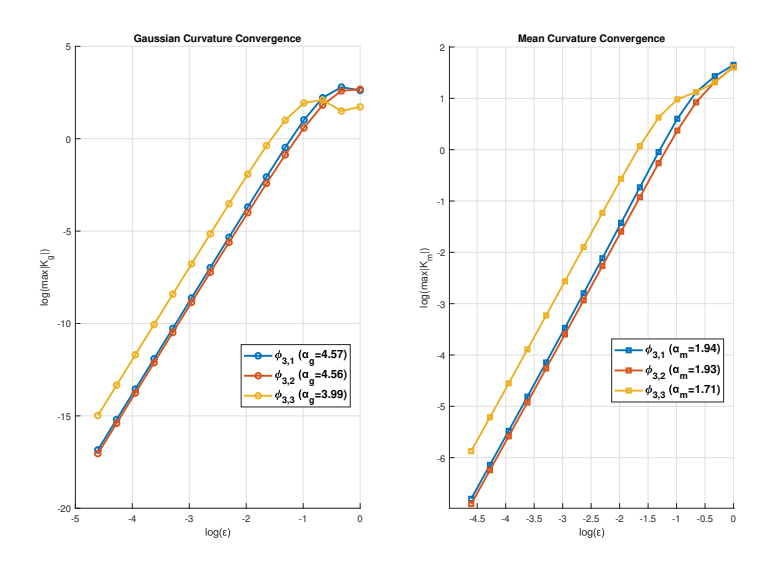


Figure 4: Convergence behavior and computed rates for Wendland RBFs.

4.2. Test problem 1: (Planar surface)

We first examine approximation of the inclined plane

$$f_1 = (x+y)/2, \quad (x,y) \in [0,1] \times [0,1].$$

As a planar surface, this function has zero Gaussian and mean curvatures everywhere. In our first investigation, we examine scalable RBFs for approximating f_1 . Table 2 presents the L_{∞} error norms and condition numbers of the interpolation matrices for five scalable RBFs: Gaussian (GA), Multiquadric (MQ) with $\beta = \frac{1}{2}$, Hyperbolic Secant (HS), RTH, and Matérn (MT) with $\nu = 2$ across various values of N. The theoretical framework established in Section 3 predicted that scalable RBF interpolants asymptotically approach planar behavior as the shape parameter approaches zero, making them theoretically well-suited for approximating flat surfaces like f_1 . However, excessively small values of ε lead to severe numerical instability due to the growth of the interpolation matrix condition number, creating a fundamental trade-off between approximation quality and numerical stability. To navigate this challenge, we employ a practical parameter selection strategy: choosing the minimum feasible ε value that avoids triggering MATLAB's rank-condition warning (RCOND), thereby ensuring computational stability while preserving optimal approximation accuracy. This approach allows us to operate at the boundary between numerical feasibility and geometric optimality. For small values of N, the numerical results demonstrate remarkable alignment with our theoretical predictions. All RBFs can accommodate relatively small shape parameters while maintaining numerical stability, enabling them to closely approach the flat limit behavior predicted by theory. The Matérn RBF exhibits exceptional performance in this regime, achieving the smallest approximation errors. This superior accuracy stems directly from the slow convergence properties identified in our curvature analysis. The Matérn slow convergence rates allow it to operate with much smaller shape parameters than other RBFs while avoiding excessive flattening. Consequently, even at these small ε values, the Matérn interpolant maintains sufficient geometric richness to provide highly accurate approximations. As N increases, numerical stability becomes the dominant constraint.

The Matérn RBF continues to outperform other kernels. The key advantage here is that while other RBFs are forced to use much larger shape parameters, resulting in more "spiky" behavior that deviates from the ideal flat limit, the Matérn RBF can still operate with relatively small parameters due to its inherent numerical stability characteristics. The numerical results provide compelling validation of our theoretical framework. Figures 5 and 6 present the L_{∞} error norms and condition numbers of interpolation matrices for the Matérn and Wendland interpolants with different RBF parameters when approximating f_1 across varying point densities, respectively. The results reveal the superiority of the Matérn RBF which is in agreement with the convergence rates reported in Figures 3 and 4, respectively. Finally, Figure 7 illustrates the L_{∞} error norms and condition numbers of interpolation matrices for the augmented polynomial-RBF interpolant using radial powers ($\beta = 3$) and TPS (n = 2) when approximating f_1 across different point densities. As demonstrated in the figure, these interpolants clearly achieve exact reproduction of f_1 .

$\phi(r)$	N	ε	L_{∞}	cond
GA	9	3.0e - 02	4.3e - 05	1.9e + 15
	25	4.4e - 01	6.7e - 05	1.7e + 15
	81	2.0e + 00	2.9e - 04	1.4e + 15
	289	5.3e + 00	1.3e - 03	1.6e + 15
	1089	1.2e + 01	2.1e - 03	9.8e + 13
MQ	9	2.8e - 02	1.4e - 05	2.2e + 15
	25	2.8e - 01	7.7e - 06	2.1e + 15
	81	9.8e - 01	8.0e - 06	1.9e + 15
	289	2.4e + 00	1.1e - 05	1.1e + 15
	1089	5.1e + 00	4.3e - 06	2.6e + 15
HS	9	2.9e - 02	2.9e - 05	2.4e + 15
	25	3.4e - 01	2.6e - 05	1.5e + 15
	81	1.3e + 00	5.1e - 05	4.8e + 14
	289	3.0e + 00	7.2e - 05	9.4e + 14
	1089	6.2e + 00	4.5e - 05	1.5e + 15
RTH	9	7.4e - 03	1.4e - 06	2.2e + 15
	25	2.7e - 01	6.6e - 06	1.3e + 15
	81	1.2e + 00	1.5e - 05	1.6e + 15
	289	3.1e + 00	2.8e - 05	7.8e + 14
	1089	6.6e + 00	1.2e - 05	2.3e + 15
МТ	9	1.1e - 03	1.9e - 07	2.3e + 15
	25	3.2e - 03	1.6e - 07	3.0 + 15
	81	8.8e - 03	1.7e - 07	3.7e + 15
	289	2.5e - 02	1.8e - 07	3.4e + 15
	1089	7.0e - 02	9.1e - 08	3.5e + 15

Table 2: L_{∞} error norms, condition numbers of interpolation matrices and the minimum ε value that avoids triggering MATLAB's RCOND warning of scalable RBF interpolants for approximation of f_1 with different values of N; Test problem 1.

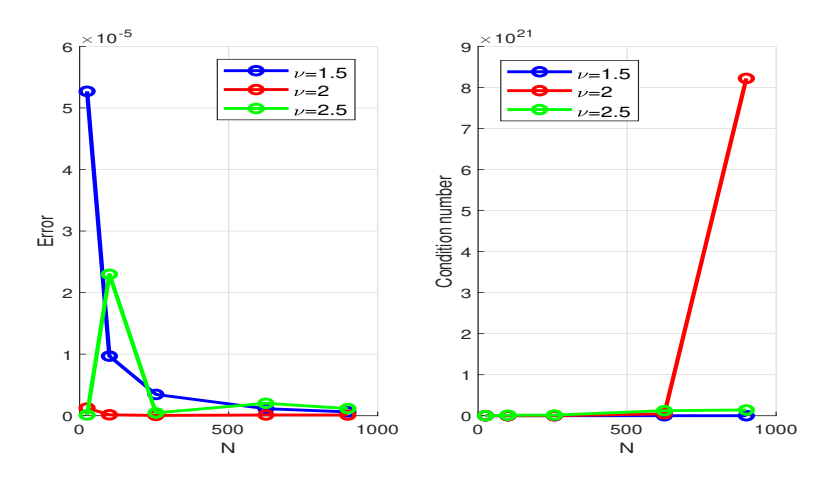


Figure 5: L_{∞} error norms and condition numbers of interpolation matrices for the Matérn interpolant when approximating f_1 with different values of N, $\varepsilon = 0.01$.

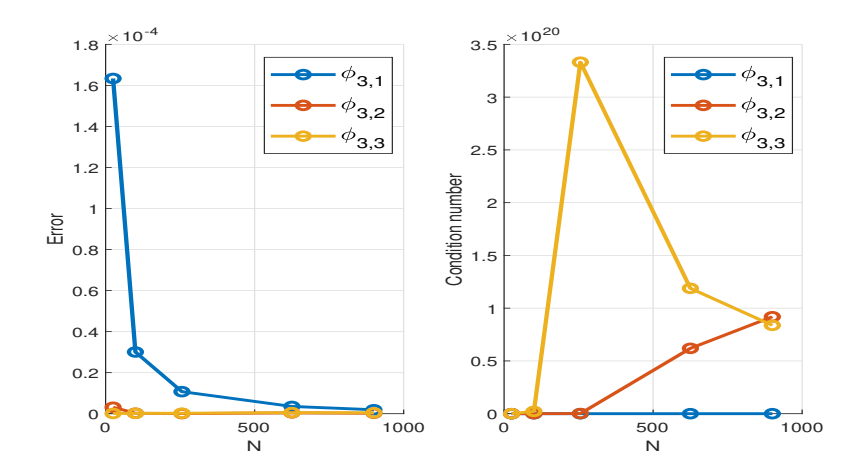


Figure 6: L_{∞} error norms and condition numbers of interpolation matrices for the Wendland interpolant when approximating f_1 with different values of N, $\varepsilon = 0.01$.

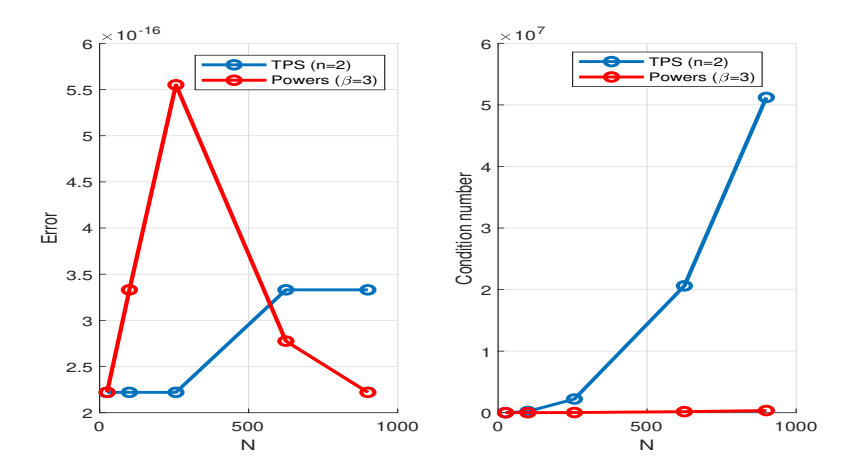


Figure 7: L_{∞} error norms and condition numbers of interpolation matrices for the augmented polynomial-RBF interpolant using radial powers ($\beta = 3$) and TPS (n = 2) when approximating f_1 with different values of N.

4.3. Test problem 2 (Steep-to-flat transition surface)

We examine the challenging test function

$$f_2 = \tanh(30(x+y)), \quad (x,y) \in [0,1] \times [0,1],$$

which is a sigmoid-like transition surface that the factor 30 creates very rapid transitions from approximately -1 to +1. But since the domain is $[0,1] \times [0,1]$, this transition occurs near the corner (0,0). Figure 8 shows the surface plot of f_2 , clearly illustrating the rapid sigmoid transition from the steep region near $x + y \approx 0$ to the flat plateau where $x + y \gg 0$. This type of surface is commonly used as a benchmark test function for interpolation methods because it combines smooth mathematical properties with challenging numerical characteristics, the "steep" and "flat" scenario. To quantify the geometric complexity, we compute its Gaussian and mean curvatures, respectively by [16]

$$K_g = \frac{f_{xx} \cdot f_{yy} - f_{xy}^2}{(1 + f_x^2 + f_y^2)^2} = 0,$$

$$K_m = \frac{f_{xx}(1 + f_y^2) + f_{yy}(1 + f_x^2) - 2f_{xy}f_xf_y}{2(1 + f_x^2 + f_y^2)^{3/2}} = \frac{-1800 \tanh(30(x+y)) \operatorname{sech}^2(30(x+y))}{(1 + 1800 \operatorname{sech}^4(30(x+y)))^{3/2}}.$$

The Gaussian and mean curvatures are plotted in Figure 9. The Gaussian curvature is zero everywhere, because f_2 depends only on the single variable (x + y). Such surfaces are called developable surfaces; they can be "unrolled" onto a plane without distortion. Actually, it is like a "bent cylinder". Unlike Gaussian curvature, $K_m \neq 0$, capturing the surface's actual bending behavior. Maximum absolute values occur where $x + y \approx 0$, in the steep sigmoid transition. K_m approaches zero exponentially as we move away from the transition $(x + y \gg 0)$. K_m changes sign across the transition, indicating the surface curves in opposite directions on either side.

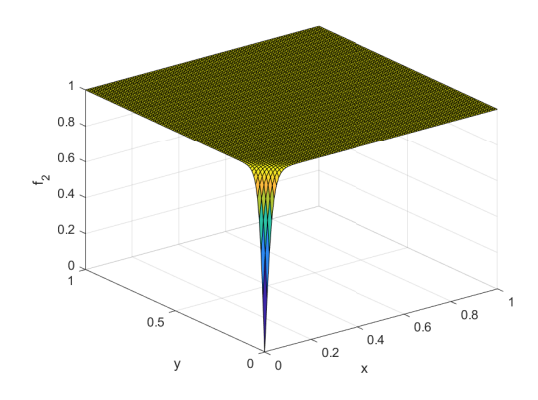


Figure 8: Plot of f_2 ; Test problem 2.

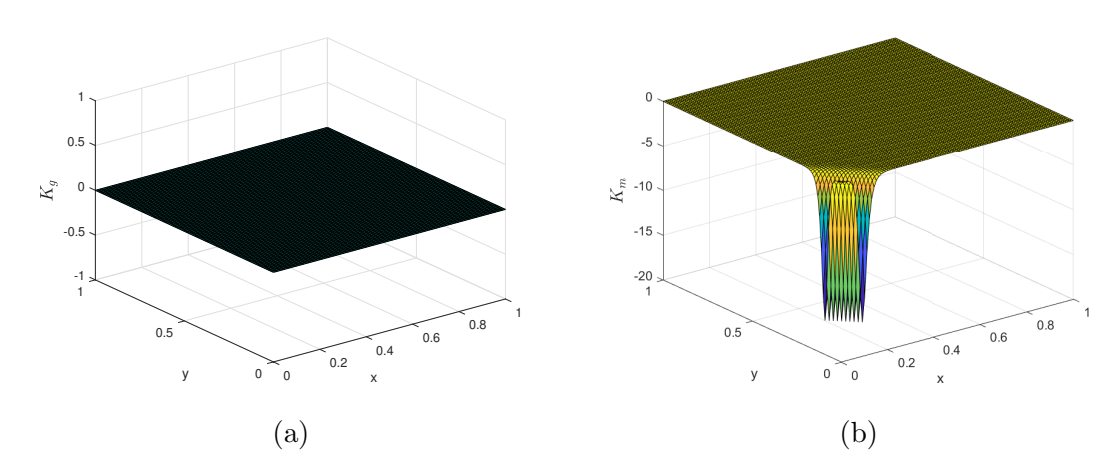


Figure 9: Gaussian (a) and mean (b) curvatures of f_2 ; Test problem 2.

For functions that exhibit both steep and flat regions, achieving a smooth global approximation requires careful consideration of the interpolation method. Two approaches are particularly effective: (1) conditionally positive definite polyharmonic functions such as TPS and radial powers, which offer scale invariance while allowing the polynomial component to capture flat regions; or (2) scalable RBFs with slowly converging curvature measures as $\varepsilon \to 0$, such as Matérn functions. The latter approach is especially advantageous because can effectively approximate both steep and gentle gradient surfaces using moderate shape parameter values and reasonable numbers of data points, without requiring excessively small values of ε . Figures 10 and 11 present the L_{∞} error norms and condition numbers of interpolation matrices for augmented polynomial-radial powers and polynomial-TPS interpolants when approximating f_2 , respectively. The numerical results demonstrate improved accuracy as both the power parameter β (or n) and the number of data points N increase simultaneously, providing empirical support for the theoretical framework outlined in Section 3.1. Furthermore, these figures confirm the expected trade-off: for a fixed number of points N, increasing β (or n) yields flatter RBFs, which consequently leads to higher condition numbers for the interpolation matrix. Figure 12 examines the interpolation error behavior of Gaussian, RTH, Matérn ($\nu = 2$), and Wendland (k = 3) interpolants when approximating f_2 using 1089 uniformly distributed points across a wide range of

shape parameter values ε . The results reveal strikingly different stability characteristics among the RBF types. While all methods achieve comparable accuracy for large ε values, both Gaussian and RTH interpolants exhibit catastrophic performance degradation as ε decreases below critical thresholds. This observation provides compelling empirical validation of the theoretical framework established in Section 3 and the curvature convergence analysis presented earlier. The catastrophic failure of Gaussian and RTH interpolants for small ε values demonstrates the practical consequences of rapid curvature convergence, wherein the interpolation matrices become severely ill-conditioned and the approximation space degenerates to inadequate polynomial subspaces. Notably, the superior performance of the Matérn RBF directly stems from its slower curvature convergence rate compared to the Wendland RBF, as predicted by our theoretical analysis. Figures 13–14 investigate the convergence behavior with respect to the number of interpolation points N for fixed shape parameters $\varepsilon = 10$ and $\varepsilon = 0.1$, respectively. For the large shape parameter case ($\varepsilon = 10$, Figure 13), all four interpolants demonstrate stable and consistent convergence behavior as N increases, with error decreasing monotonically for each method. The small shape parameter case ($\varepsilon = 0.1$, Figure 14) reveals the critical importance of curvature convergence rates in practical applications. In this regime, the fundamental differences in curvature convergence behavior manifest as dramatically different performance characteristics. The Matérn and Wendland interpolants continue to exhibit stable, monotonic error reduction with increasing N, maintaining their reliability even in this challenging parameter range. In stark contrast, both Gaussian and RTH interpolants fail catastrophically in this regime, exhibiting unstable and erratic behavior with errors that neither converge nor remain within acceptable bounds as N increases. These failures directly validate our theoretical predictions that RBFs with rapid curvature convergence become impractical for small shape parameters due to excessive flattening and severe matrix ill-conditioning. Importantly, the Matérn RBF achieves higher accuracy than the Wendland RBF across various values of N, further demonstrating the practical advantages conferred by its slower curvature convergence rate. These results establish the Matérn RBF as the preferred choice for complex surface approximation tasks, particularly when working with small shape parameters or large point sets where competing methods fail due to fundamental limitations in their curvature convergence behavior.

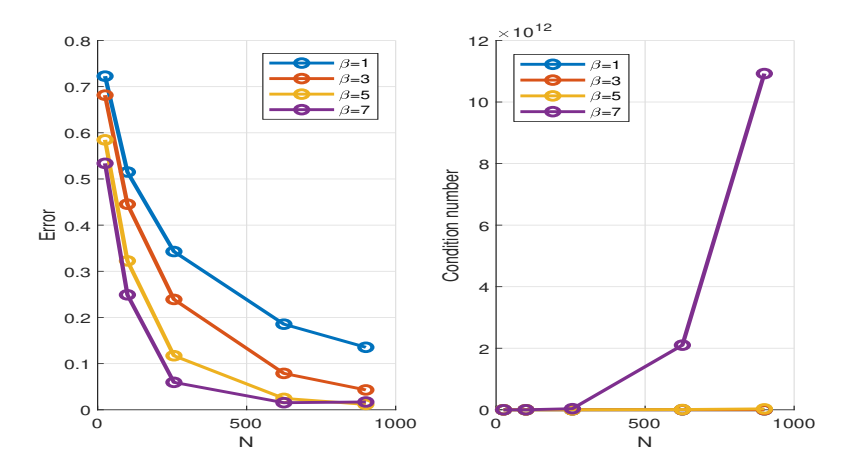


Figure 10: L_{∞} error norms and condition numbers of interpolation matrices for the augmented polynomial-radial powers interpolant, when approximating f_2 with different values of N.

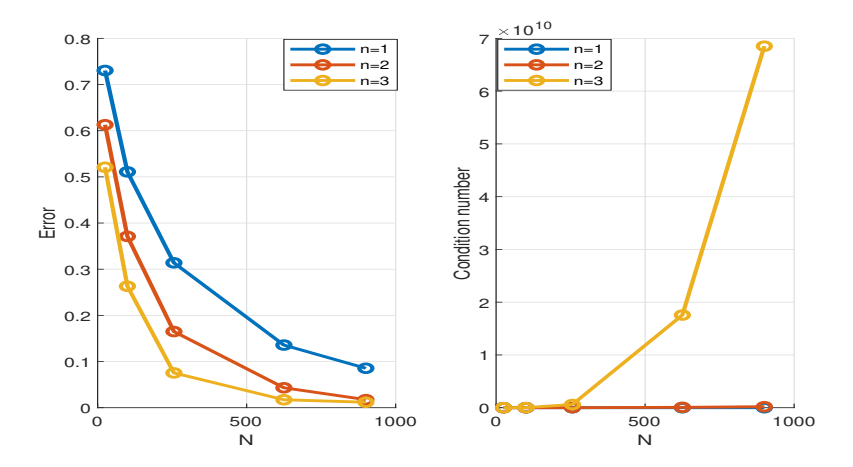


Figure 11: L_{∞} error norms and condition numbers of interpolation matrices for the augmented polynomial-TPS interpolant, when approximating f_2 with different values of N.

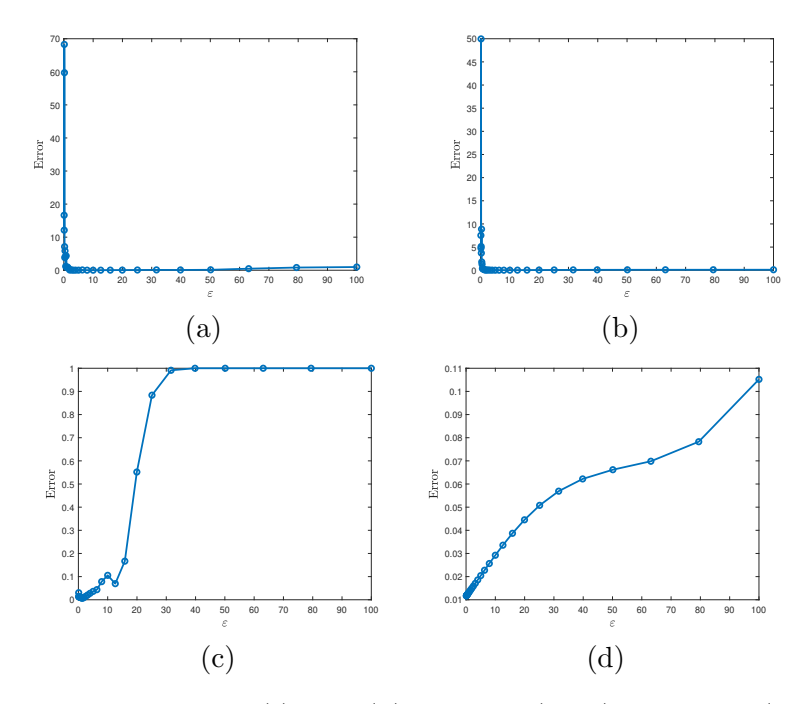


Figure 12: Error distribution of Gaussian (a), RTH (B), Wendland (k=3), and Matérn ($\nu=2$) (d) interpolants for approximating f_2 with 1089 uniform points and different values of ε ; Test problem 2.

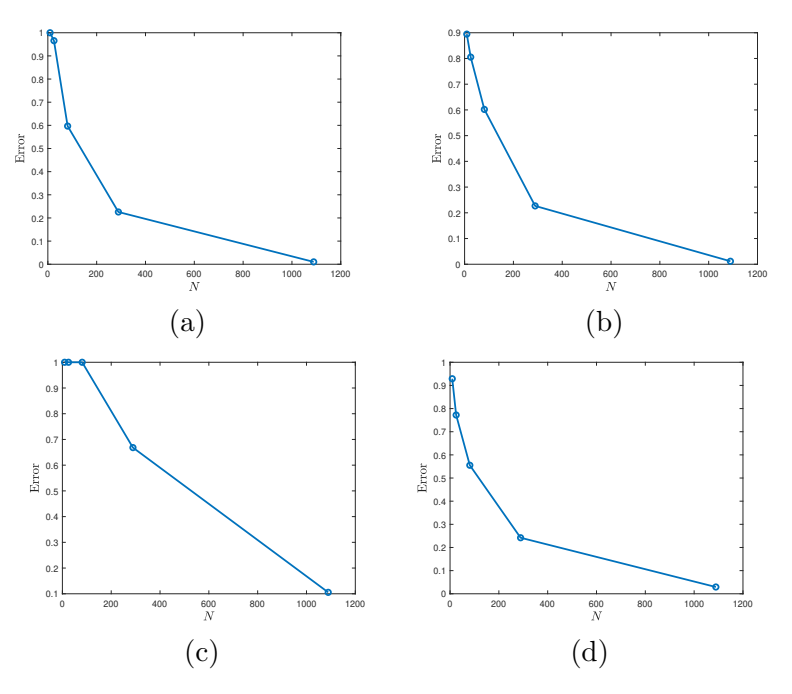


Figure 13: Error distribution of Gaussian (a), RTH (b), Wendland (k=3) (c), and Matérn ($\nu=2$) (d) interpolants for approximating f_2 with $\varepsilon=10$ and different values of N; Test problem 2.

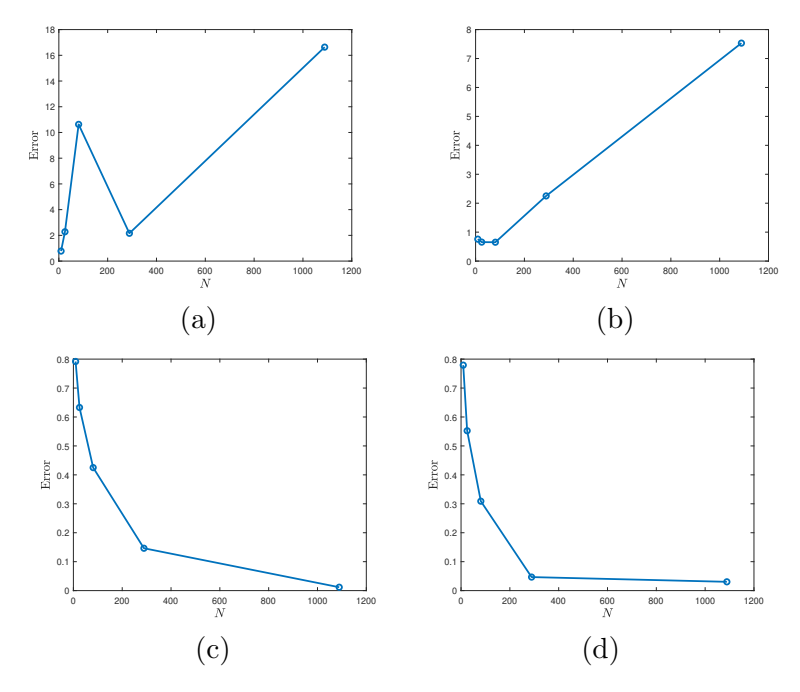


Figure 14: Error distribution of Gaussian (a), RTH (b), Wendland (k=3) (c), and Matérn ($\nu=2$) (d) interpolants for approximating f_2 with $\varepsilon=0.1$ and different values of N; Test problem 2.

5. Conclusion

We have developed a differential geometric framework for analyzing RBFs by interpreting them as surfaces of revolution, enabling the derivation of curvature-based metrics that effectively predict interpolation accuracy and numerical stability. The fundamental distinction between scalable and unscalable RBFs emerges naturally from their curvature characteristics at the origin. Our investigation reveals that curvature convergence rates as shape parameters approach zero serve as reliable indicators of practical performance. The systematic analysis demonstrates a clear hierarchy among scalable RBFs: Matérn functions exhibit the slowest convergence rates, followed by Wendland functions, while Gaussian, Multiquadric, Hyperbolic Secant, and RTH RBFs converge rapidly with nearly identical rates. Among Matérn functions, $\nu = 2$ demonstrates the slowest convergence, and among Wendland functions, $\phi_{3,3}$ maintains a richer approximation space. The numerical experiments validate these theoretical predictions across two distinct test problems. For planar surface approximation, numerical results demonstrate that the Matérn RBF achieves errors several orders of magnitude lower than competing scalable RBFs, while unscalable functions augmented with polynomials provide exact reproduction. For the challenging steep-to-flat transition surface, numerical experiments reveal dramatically different behaviors: Matérn and Wendland interpolants maintain stable, monotonic error reduction across all parameter regimes, while Gaussian and RTH interpolants suffer catastrophic failure for small shape parameters due to excessive flattening and severe matrix ill-conditioning. Also, the Matérn RBF achieves noticeably higher accuracy than Wendland functions across various values of N, directly confirming the practical advantages conferred by its slower curvature convergence rate. The geometric perspective also clarifies the behavior of unscalable functions. Thin plate splines and radial powers, when properly augmented with polynomial components, demonstrate inherent stability independent of any scaling parameter. This differential geometric framework provides practitioners with rigorous theoretical guidance for RBF selection, replacing ad-hoc parameter tuning with principled design choices based on intrinsic surface properties. The slow curvature convergence criterion emerges as a fundamental principle for identifying superior RBF kernels. Future research directions include extending this geometric analysis to higher dimensions, establishing quantitative relationships between curvature convergence rates and approximation error bounds, developing adaptive shape parameter selection strategies based on local curvature measures, and exploring the design of new RBF families with tailored curvature convergence properties optimized for specific application domains.

Appendix A. Differential geometric basics

Here, we give an account of the differential geometry basics that are in our focus [13, 25, 35].

Definition Appendix A.1. A patch or local surface is a differentiable mapping

$$\sigma: \mathcal{U} \longrightarrow \mathbb{R}^n$$
,

where \mathcal{U} is an open subset of \mathbb{R}^2 .

It can be written as an *n*-tuple of functions

$$\sigma(u,v) = (\sigma_1(u,v), \dots, \sigma_n(u,v)).$$

The first order partial derivative of σ with respect to u is given by $\sigma_u = \left(\frac{\partial \sigma_1}{\partial u}, \dots, \frac{\partial \sigma_n}{\partial u}\right)$. The other partial derivatives are defined similarly.

Definition Appendix A.2. A regular parametrization of a subset $\mathcal{M} \subset \mathbb{R}^3$ is a C^1 one-to-one patch $\sigma: \mathcal{U} \to \mathcal{M} \subset \mathbb{R}^3$ with the continuous inverse $\sigma^{-1}: \sigma(\mathcal{U}) \to \mathcal{U}$ such that

$$\sigma_u \times \sigma_v \neq 0$$
.

A connected subset $\mathcal{M} \subset \mathbb{R}^3$ is called a regular surface if each point has a neighborhood that is regularly parametrized.

Theorem Appendix A.3. ([1]). Let $\mathcal{U} \subset \mathbb{R}^2$ be open. Then if a function $g: \mathcal{U} \to \mathbb{R}$ is differentiable, the subset $\mathcal{M} := \{(x, y, z)^\mathsf{T} \in \mathbb{R}^3 | z = g(x, y)\}$ is a regular surface.

Proof. The graph of the function g, is parametrized by $\sigma(u,v)=(u,v,g(u,v))$. Then $\sigma_u\times\sigma_v=(-g_u,-g_v,1)\neq 0$.

Definition Appendix A.4. A regular surface is called of class C^r if all the systems of coordinates σ are of class C^r .

Definition Appendix A.5. The tangent plane of the regular surface \mathcal{M} at the point $p = \sigma(u_0, v_0)$ is the set of all possible tangent vectors to curves in \mathcal{M} at p. That is

$$T_p\mathcal{M} = \operatorname{span}\{\sigma_{\mathbf{u}}(\mathbf{u}_0, \mathbf{v}_0), \sigma_{\mathbf{v}}(\mathbf{u}_0, \mathbf{v}_0)\} \subset \mathbb{R}^3.$$

Definition Appendix A.6. The unit normal $\vec{n}(u, v)$ to a regular surface is defined by

$$\vec{n}(u, v) = \frac{\sigma_u \times \sigma_v}{\|\sigma_u \times \sigma_v\|}\Big|_{(u, v)},$$

at those points $(u, v) \in \mathcal{U}$ at which $\sigma_u \times \sigma_v$ does not vanish.

A visual representation of the above notions is given in Figure A.15. In order to measure

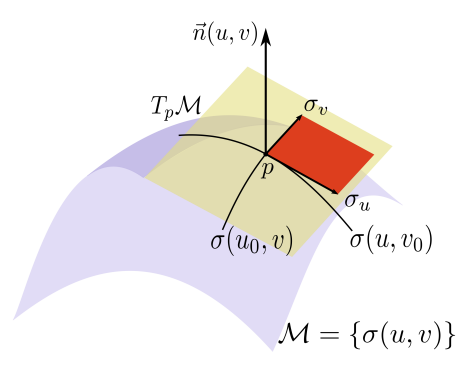


Figure A.15: Surface \mathcal{M} with the regular parametrization σ , normal vector $\vec{n}(u, v)$, and tangent plane $T_p(\mathcal{M})$.

how a regular surface \mathcal{M} bends in \mathbb{R}^3 , we need to estimate how its normal \vec{n} changes from point to point. So the following linear operator called the shape operator is used to calculate the bending of \mathcal{M} .

Definition Appendix A.7. The shape operator S_p at the tangent vector ω is the negative of the derivative of \vec{n} in the direction ω :

$$S_p: T_p(\mathcal{M}) \longrightarrow T_p(\mathcal{M})$$

 $S_p(\omega) = -D_{\omega}\vec{n}.$

Lemma Appendix A.8. ([13]). For a regular surface patch σ about point p, we have

$$S_p(\sigma_u) = -\vec{n}_u$$
 and $S_p(\sigma_v) = -\vec{n}_v$,

where \vec{n}_u and \vec{n}_v are the partial derivatives of the unit normal vector \vec{n} with respect to the surface parameters u and v.

Definition Appendix A.9. The symmetric bilinear function

$$I_p: T_p(\mathcal{M}) \times T_p(\mathcal{M}) \to \mathbb{R},$$

defined by

$$I_p(v, w) = v \cdot w,$$

is called the first fundamental form.

The first fundamental form encodes the "intrinsic data" about the surface i.e., the information that one could discover by wandering around on the surface and making measurements within the surface.

Lemma Appendix A.10. ([35]). Let $\sigma: \mathcal{U} \longrightarrow \mathbb{R}^3$ be a regular surface patch about point p. Then

$$I_p(a_1\sigma_u + a_2\sigma_v, b_1\sigma_u + b_2\sigma_v) = \begin{pmatrix} a_1 & a_2 \end{pmatrix} \begin{pmatrix} E & F \\ F & G \end{pmatrix} \begin{pmatrix} b_1 \\ b_2 \end{pmatrix};$$

where $E = \sigma_u \cdot \sigma_u$, $F = \sigma_u \cdot \sigma_v$, and $G = \sigma_v \cdot \sigma_v$.

Definition Appendix A.11. Let \mathcal{M} be a regular surface of class C^2 in \mathbb{R}^3 . The symmetric bilinear function

$$\mathbf{II}_p: T_p(\mathcal{M}) \times T_p(\mathcal{M}) \to \mathbb{R},$$

defined by

$$\mathbf{II}_{p}(v, w) = S_{p}(v) \cdot w,$$

is called the second fundamental form.

The second fundamental form, on the other hand, encodes the information about how the surface is embedded into the surrounding three-dimensional space explicitly, it tells how the normal vector to the surface varies as one moves in different directions on the surface.

Lemma Appendix A.12. ([35]). Let $\sigma: \mathcal{U} \longrightarrow \mathbb{R}^3$ be a regular surface patch about p. Then

$$\mathbb{I}_p(a_1\sigma_u + a_2\sigma_v, b_1\sigma_u + b_2\sigma_v) = \begin{pmatrix} a_1 & a_2 \end{pmatrix} \begin{pmatrix} L & M \\ M & N \end{pmatrix} \begin{pmatrix} b_1 \\ b_2 \end{pmatrix};$$

where $L = \sigma_{uv} \cdot \vec{n}$, $M = \sigma_{uv} \cdot \vec{n}$, and $N = \sigma_{vv} \cdot \vec{n}$.

Theorem Appendix A.13. ([35]). The matrix of the linear map S_p with respect to the basis $\{\sigma_u, \sigma_v\}$ is given by

$$[S_p] = [I_p]^{-1}[\mathbf{II}_p] = \begin{bmatrix} E & F \\ F & G \end{bmatrix}^{-1} \begin{bmatrix} L & M \\ M & N \end{bmatrix}.$$

Then the symmetric matrices corresponding to the first and second fundamental forms, and the shape operator, are given respectively by

$$[\mathbf{I}_p] = \begin{bmatrix} E & F \\ F & G \end{bmatrix}, \quad [\mathbf{II}_p] = \begin{bmatrix} L & M \\ M & N \end{bmatrix}, \quad \text{and} \quad [S_p] = [\mathbf{I}_p]^{-1}[\mathbf{II}_p].$$

By the Spectral Theorem [26], $[S_p]$ has two real eigenvalues, which are called principal curvatures and are denoted by k_1 and k_2 .

Definition Appendix A.14. Let \mathcal{M} be a regular surface of class C^2 in \mathbb{R}^3 . The Gaussian curvature K_q and mean curvature K_m of \mathcal{M} are the functions $K_q, K_m : \mathcal{M} \longrightarrow \mathbb{R}$ defined by

$$K_g = \det([S_p]) = k_1 k_2,$$
 and $K_m = \frac{1}{2} \operatorname{tr}([S_p]) = \frac{1}{2} (k_1 + k_2).$

Now, Theorem Appendix A.13 results

$$K_g = \frac{\det([\mathbb{I}_p])}{\det([\mathbb{I}_p])} = \frac{LN - M^2}{EG - F^2},$$

$$K_m = \frac{1}{2} \frac{LG - 2MF + NE}{EG - F^2}.$$

Gaussian curvature captures the intrinsic "bendiness" of a surface. It tells whether a surface curves away from being flat in a fundamental way. A sphere has positive Gaussian curvature everywhere because it curves outward in all directions, while a saddle shape has negative Gaussian curvature because it curves up in one direction and down in the perpendicular direction.

Mean curvature, on the other hand, measures how much a surface deviates from being flat on average across different directions at each point. It's more about the surface's tendency to curve toward one side or another. Surface shapes can be identified by the sign of the Gaussian and mean curvatures (see [35] for more details).

Definition Appendix A.15. A regular surface is is said to be flat if its Gaussian curvature vanishes identically.

Proposition Appendix A.16. ([35]). If the shape operator S_p is 0 for all $p \in \mathcal{M}$ or equivalently, if both K_g and K_m vanish identically on the surface, then the surface is a part of a plane.

Theorem Appendix A.17 (Gauss's Theorema Egregium [35]). The Gaussian curvature is determined only by the first fundamental form I_p .

According to Theorem Appendix A.17, if we change the surface while preserving lengths and angles in the surface, the Gaussian curvature does not change. More generally, if two surfaces are locally isometric, their Gaussian curvatures at corresponding points are equal. For example, the plane and cylinder are locally isometric, and hence the cylinder is flat. Since the Gaussian curvature of a sphere is nonzero, a sphere cannot be locally isometric to a plane.

The following theorem plays a crucial role in the framework of our investigation.

Theorem Appendix A.18 (Fundamental Theorem of Surface Theory [35]). Two parametrized surfaces $\sigma, \sigma^* : \mathcal{U} \longrightarrow \mathbb{R}^3$ are congruent (i.e., differ by the composition of a translation and a rotation) if and only if $I_p = I_p^*$ and $I_p = \pm I_p^*$.

Appendix B. Surfaces of Revolution

Surfaces of revolution, generated by rotating a curve around a fixed axis, are a fundamental class of surfaces in differential geometry with broad applications across engineering, architecture, art, and design. Their main advantage lies in the simplicity of their parametrization, often described by straightforward equations that facilitate calculations of surface area, volume, and curvature. The inherent symmetry reduces complex problems to one-dimensional integrals, streamlining analysis. Studying these surfaces deepens our understanding of curved geometries and their intrinsic properties, making them a valuable and versatile tool in both theoretical and practical contexts.

Definition Appendix B.1. Let $I \subset \mathbb{R}$ be an interval, and let $\alpha(u) = (0, g(u), h(u)), u \in I$, be a regular parametrized plane curve with g > 0. Then the surface of revolution obtained by rotating α about the z-axis is parametrized by

$$\sigma(u, v) = (g(u)\cos v, g(u)\sin v, h(u)), \quad u \in I, \ 0 \le v < 2\pi.$$

Theorem Appendix B.2. ([25]). A flat surface of revolution is part of a plane, cone, or cylinder.

References

- [1] T. F. Banchoff and S. Lovett. *Differential geometry of curves and surfaces*. Chapman and Hall/CRC, 2022.
- [2] V. Bayona. An insight into rbf-fd approximations augmented with polynomials. *Computers & Mathematics with Applications*, 77(9):2337–2353, 2019.
- [3] M. Bozzini, L. Lenarduzzi, M. Rossini, and R. Schaback. Interpolation with variably scaled kernels. *IMA Journal of Numerical Analysis*, 35(1):199–219, 2015.
- [4] M. Bozzini, L. Lenarduzzi, and R. Schaback. Adaptive interpolation by scaled multi-quadrics. *Adv. Comput. Math.*, 16(4):375–387, 2002.
- [5] R. Cavoretto, A. De Rossi, M. S. Mukhametzhanov, and Y. D. Sergeyev. On the search of the shape parameter in radial basis functions using univariate global optimization methods. J. Global Optim., 79(2):305–327, 2021.
- [6] R. Cavoretto, A. De Rossi, and E. Perracchione. Optimal selection of local approximants in RBF-PU interpolation. *J. Sci. Comput.*, 74(1):1–22, 2018.
- [7] S. De Marchi, F. Marchetti, and E. Perracchione. Jumping with variably scaled discontinuous kernels (vsdks). *BIT Numerical Mathematics*, 60(2):441–463, 2020.
- [8] G. E. Fasshauer. Meshfree approximation methods with MATLAB, volume 6. World Scientific, 2007.
- [9] G. E. Fasshauer and M. J. McCourt. Kernel-based Approximation Methods Using MATLAB, volume 19 of Interdisciplinary Mathematical Sciences. World Scientific, Singapore, 2015.
- [10] G. E. Fasshauer and J. G. Zhang. On choosing "optimal" shape parameters for RBF approximation. *Numer. Algor.*, 45(1-4):345–368, 2007.
- [11] B. Fornberg and G. Wright. Stable computation of multiquadric interpolants for all values of the shape parameter. *Computers & Mathematics with Applications*, 48(5-6):853–867, 2004.
- [12] B. Fornberg and J. Zuev. The Runge phenomenon and spatially variable shape parameters in RBF interpolation. *Comput. Math. Appl.*, 54(3):379–398, 2007.
- [13] A. Gray, E. Abbena, S. Salamon, et al. Modern differential geometry of curves and surfaces with Mathematica. CRC press, 2006.
- [14] M. Heidari, M. Mohammadi, and S. De Marchi. A shape preserving quasi-interpolation operator based on a new transcendental RBF. *Dolomites Research Notes on Approximation*, 14(1):56–73, 2021.
- [15] M. Heidari, M. Mohammadi, and S. De Marchi. Curvature based characterization of radial basis functions: application to interpolation. *Mathematical Modelling and Analysis*, 28(3):415–433, 2023.
- [16] Y.-B. Jia. Gaussian and mean curvatures. Com S, 477(577):1-7, 2020.

- [17] E. Kansa and R. Carlson. Improved accuracy of multiquadric interpolation using variable shape parameters. *Comput. Math. Appl.*, 24(12):99–120, 1992.
- [18] E. Larsson and B. Fornberg. A numerical study of some radial basis function based solution methods for elliptic pdes. *Computers & Mathematics with Applications*, 46(5-6):891–902, 2003.
- [19] L. Ling and F. Marchetti. A stochastic extended rippa's algorithm for lpocv. Applied Mathematics Letters, 129:107955, 2022.
- [20] F. Marchetti. The extension of rippa's algorithm beyond loocy. *Applied Mathematics Letters*, 120:107262, 2021.
- [21] P. K. Mishra, G. E. Fasshauer, M. K. Sen, and L. Ling. A stabilized radial basis-finite difference (RBF-FD) method with hybrid kernels. *Computers & Mathematics with Applications*, 77(9):2354–2368, 2019.
- [22] P. K. Mishra, S. K. Nath, M. K. Sen, and G. E. Fasshauer. Hybrid gaussian-cubic radial basis functions for scattered data interpolation. *Computational geosciences*, 22(5):1203– 1218, 2018.
- [23] M. Mohammadi, A. Sommariva, and M. Vianello. Unisolvence of kansa collocation for elliptic equations by polyharmonic splines with random fictitious centers. *Applied Mathematics Letters*, 168:109571, 2025.
- [24] M. Mohammadi, A. Sommariva, and M. Vianello. Unisolvence of randomized multiquadric kansa collocation for convection—diffusion with mixed boundary conditions: M. mohammadi et al. *Mediterranean Journal of Mathematics*, 22(6):144, 2025.
- [25] B. O'neill. Elementary differential geometry. Elsevier, 2006.
- [26] R. S. Palais. A modern course on curves and surfaces. Virtual Math Museum, 2011.
- [27] F. Pooladi and E. Larsson. Stabilized interpolation using radial basis functions augmented with selected radial polynomials. *Journal of Computational and Applied Mathematics*, 437:115482, 2024.
- [28] M. Powell. Radial basis function methods for interpolation to functions of many variables. In *Hercma*, pages 2–24, 2001.
- [29] S. Rippa. An algorithm for selecting a good value for the parameter c in radial basis function interpolation. Adv. Comput. Math., 11(2-3):193-210, 1999.
- [30] M. Rossini. Interpolating functions with gradient discontinuities via variably scaled kernels. Dolomites Research Notes on Approximation, 11(2), 2018.
- [31] M. Rossini. Variably scaled kernels: an overview. *Dolomites Research Notes on Approximation*, 15(4):61–72, 2022.
- [32] S. A. Sarra and Y. Bai. A rational radial basis function method for accurately resolving discontinuities and steep gradients. *Applied Numerical Mathematics*, 130:131–142, 2018.

- [33] R. Schaback. Error estimates and condition numbers for radial basis function interpolation. Advances in Computational Mathematics, 3(3):251–264, 1995.
- [34] M. Scheuerer. An alternative procedure for selecting a good value for the parameter c in RBF-interpolation. Adv. Comput. Math., 34(1):105–126, 2011.
- [35] T. Shifrin. Differential geometry: a first course in curves and surfaces. *University of Georgia*, 2015.
- $[36] \ \ H. \ \ Wendland. \ \ Scattered \ \ data \ \ approximation, \ volume \ 17. \ \ Cambridge \ university \ press, \ 2004.$